RSC Advances

PAPER

View Article Online
View Journal | View Issue

Cite this: *RSC Adv.*, 2021, **11**, 37528

Modifying Y zeolite with chloropropyl for improving Cu load on Y zeolite as a super Cu/Y catalyst for toluene oxidation†

Xiaoling Meng,[a] Lingke Meng,[a] Yanjun Gong, *[a] Zhihong Li,*[b] Guang Mo[b] and Jing Zhang[b]

Developing an efficient catalyst is desirable when for example moving from a noble metal-based catalyst to a transition metal-based one for VOC removal. In this work, the chloropropyl-modified NaY zeolite (NaY-CPT) was first synthesized in an extremely dense system through introducing 3-chloropropyl-trimethoxysilane (CPT) in the aluminosilicate sol. Then the Cu/Y-CPT catalyst was fabricated by impregnating Cu species on the NaY-CPT zeolite and the highly effective Cu/Y based catalyst has been achieved for catalytic toluene oxidation. The structure evolution of CPT modified sol and its effect on texture properties of NaY-CPT and thereby reduction ability of Cu/Y catalyst were systematically investigated by synchrotron radiation small angle X-ray scattering (SR-SAXS), EXAFS and other characterization. The CPT modified sol can promote the formation of more active aluminosilicate species, greatly accelerating crystal growth and improving framework Si/Al ratio of NaY zeolite. Due to the presence of the CPT group, the Cu/Y-CPT catalyst enhanced the interaction between Cu species and the zeolite matrix, resulting in small sized CuO nanoparticles (2.0–4.0 nm) anchoring to NaY-CPT. The Cu/Y-CPT catalyst renders more isolated Cu^{2+} species and adsorbed oxygen species, which are reactive in the oxidation reaction due to their high reducibility and mobility. Finally, the Cu/Y-CPT catalyst exhibits 90% toluene conversion at 296 °C (T_{90}), lower than the value of 375 °C on the conventional Cu/Y-con catalyst. Meanwhile, the optimal Cu/Y-CPT catalyst also gives higher toluene conversion and stability in moisture conditions.

Received 27th August 2021
Accepted 14th November 2021

DOI: 10.1039/d1ra06469j

rsc.li/rsc-advances

1 Introduction

Volatile organic compounds (VOCs) are chemical compounds which present a high vapor pressure and a low boiling point at room temperature, resulting in a large number of molecules to evaporate or sublimate from the compound into the surrounding air. VOCs principally come from combustion engines, industrial emissions and domestic products.

Many VOCs are hazardous to human health or to the environment. For instance, toluene as a typical aromatic VOC, significantly contributes to industrial and daily life pollutants. It has been well recognized as a highly polluting molecule because of its high Photochemical Ozone Creativity Potential (POCP).[1,2] Therefore, it is usually a model compound to be evaluated in the research process.

Among the available VOC elimination techniques such as adsorption, thermal incineration, biological degradation and catalytic oxidation *et al.*,[3–5] the catalytic oxidation in the presence of catalyst has prominent advantages of both high efficiency and less pollution because it can completely convert organic pollutants into harmless species like CO_2 and H_2O at relatively low temperatures.[6,7] Noble metal supported catalysts, such as Pt/Beta, Pd/Hβ,[8,9] transition metal oxides *i.e.* Co_3O_4, MnO_x,[10–12] bronzes,[13] as well as mixed oxides are active in the VOCs oxidation reaction.[14–16] The noble metal catalysts showed super-performance for VOCs elimination, but the wide application is limited due to their high cost, low thermal stability, easy sintering and sensibility to poisoning.[17–19] As a result, transition metal-based catalysts have attracted great attention because of economic viability and poison tolerance in industrial applications.[20–22]

Zeolite features large surface areas, high adsorption capacity and high thermal/hydrothermal stability, which is considered as one of the most potential supports for the VOCs abatement.[21,23] Some promising strategies based on a combination of transition metal and zeolite have been established.[24,25] For example, Soylu *et al.* prepared clinoptilolite zeolite (CLT) supported Cu, Fe, Co and Mn transition metals as toluene oxidation catalysts, showing that the Mn-CLT catalyst exhibits a high

[a]*State Key Laboratory of Heavy Oil Processing, The Key Laboratory of Catalysis of CNPC, College of Chemical Engineering, China University of Petroleum, Beijing, 102249, China. E-mail: gongyj@cup.edu.cn*

[b]*Beijing Synchrotron Radiation Laboratory, Institute of High Energy Physics, Chinese Academy of Sciences, Beijing, China. E-mail: lzh@ihep.ac.cn*

† Electronic supplementary information (ESI) available. See DOI: 10.1039/d1ra06469j

catalytic activity.[26] Meng *et al.* designed a facile one-step hydrothermal method to prepared Mn-ZSM-5 catalyst for toluene catalytic oxidation, resulting in a total toluene conversion of 65% to carbon dioxide.[27] Antunes *et al.* prepared a series of CuNaHY catalysts with different copper content and found that the catalysts with copper content from 1 to 8 wt% can promote the oxidation of toluene and facilitate the removal of coke formed in the course of reaction.[28] Romero *et al.* prepared CuX catalysts by ion exchange method. The sample with low copper content (1 wt%) exhibited promising features in terms of toluene adsorption capacity and total oxidation, owing to the presence of micropores and well-dispersed CuO species.[29] Rokicińska *et al.* confirmed that siliceous SiBEA zeolite can be used as support to form Co_3O_4/BEA catalyst, which was recognized Co_3O_4 as the main active phase in the total oxidation of toluene.[10] The catalytic activity of Cu- and Co-based beta zeolites for the toluene oxidation, in Raga and co-workers' research, showed that a proper redox property and metal–zeolite interaction both were the key factors for designing catalyst.[20] Therefore, regulating zeolite surface and structural properties are strongly desirable to improve the catalytic activities.

In this work, NaY zeolite is preferentially chosen as support because FAU type zeolite is composed of a three-dimensional (3D) 12-membered ring pore structures with high surface area and low steric restrictions, and it benefits to VOCs removal in a high throughput treatment. The most mature technology for industrial Y zeolite synthesis is hydrothermal crystallization in the dilute system by using water glass as silicon source.[30] This synthesis process that contains very low silica content leads to low zeolite yield and large amount of waste mother-liquid.[31] Herein, a new synthesis of Y zeolite was carried out by a facile organo-modified aluminosilicate sol as structure directing agent to apply for VOCs removal. Using 3-chloropropyl-trimethoxysilane (CPT) modified sol as structure directing agent, NaY-CPT zeolite was *in situ* synthesized in a condensed system using solid SiO_2 as silicon source. It not only modulates the surface properties and morphology, but also enhances NaY zeolite crystallization with high solid yield and optimal properties. Finally, NaY-CPT zeolite with an enhanced surface modification was prepared and used as support, after the subsequent Cu species immobilization, Cu/Y-CPT catalysts were obtained which performed high efficiency for total toluene oxidation.

Through systematically investigating the structure evolution of CPT modified aluminosilicate sol (sol-CPT) and its effect on NaY zeolite structure and reduction ability of Cu/Y-CPT catalysts by synchrotron radiation small angle X-ray scattering (SR-SAXS) and other techniques, the new insights into the synthesis of NaY-CPT zeolite and chemical behaviour of Cu species on the Cu/Y-CPT catalyst are provided, *i.e.*, optimal texture property of NaY-CPT zeolite, the distribution of isolated Cu^{2+}, CuO nanoparticles and its effect on catalytic performance in the toluene oxidation reaction.

2 Experimental

2.1 Catalyst preparation

Accordingly, the optimal aluminosilicate sol as structure directing agent (SDA) is an essential prerequisite for synthesis of NaY zeolite. A typical synthesis for SDA is as following: 1.45 g NaOH (99 wt%, Beijing Chemical Company) and 0.33 g $NaAlO_2$ (45 wt% Al_2O_3, 27 wt% Na_2O, Sinopharm Chemical Reagent Co., Ltd) were mixed with 4.03 g deionized water, followed by addition of 8.84 g water glass (19.82 wt% SiO_2, 6.88 wt% Na_2O, Hongxing Chemical Company) with final mixture composition of $20Na_2O : Al_2O_3 : 20SiO_2 : 400H_2O$, which was denoted as sol-con. A procedure for preparing NaY zeolite is as following. Mix 5.53 g solid silica (99 wt%, Hongxing Chemical Company) with 3.20 g sodium aluminate and 10.80 g deionized water. Then, 14.64 g SDA was added to obtain a feedstock gel with a molar composition of $3.0Na_2O : Al_2O_3 : 8.0SiO_2 : 80H_2O$. The gel was crystallized for 48 h at the temperature 100 °C. Finally, the solid was filtered and washed with deionized water, dried at 100 °C overnight.

To prepare chloropropyl-modified NaY zeolites (labeled NaY-CPT), the SDA sol was obtained by introducing 0.093–0.370 g 3-chloropropyl-trimethoxysilane (denoted as CPT, 98 wt%, Aldrich) in the conventional alumino-silicate sol (labeled sol-CPT-x, x = 0.5–2.0%, x refers to the molar ratio of 3-chloropropyl-trimethoxysilane (CPT) to solid silica).

Zeolite supported Cu (5–15 wt%) catalysts were prepared by incipient wetness impregnation method using an appropriate amount of aqueous solution of $Cu(NO_3)_2 \cdot 3H_2O$ (99 wt%, Sinopharm Chemical Reagent Co., Ltd) at room temperature. The samples were then calcined at 550 °C for 6 h under dry air flow. These calcined zeolites supported Cu catalysts were denoted as Cu/Y-5-con and Cu/Y-x-CPT (x = 5–15 wt%), respectively. All catalysts were pelletized, and then the pellets were crushed and sieved to obtain grains of 0.42–0.84 mm in diameter.

2.2 Physicochemical characterization

X-ray powder diffraction patterns (XRD) were recorded on a Shimadzu XRD-6000 diffractometer (40 kV, 30 mA) and using Ni-filtered Cu Kα radiation (λ = 1.5406 Å) at a scanning rate of 2° min^{-1} from 5° to 50° (2θ). The relative crystallinity (RC) of all samples were calculated by comparing the sum of the area of characteristic peaks at $2\theta = 15.7° \pm 0.2$, $18.7° \pm 0.2$, $20.4° \pm 0.2$, $23.7° \pm 0.2$, $27.1° \pm 0.2$, $30.8° \pm 0.2$, $31.5° \pm 0.2$ and $34.2° \pm 0.2$ with that of the standard sample.

The scanning electron microscope (SEM) was performed on a Hitachi SU8010 field-emission. Transmission electron microscopy (TEM) images were obtained using a FEI Tecnai G2 F20 instrument at an acceleration voltage of 200 kV. Fourier transform infrared (FT-IR) spectra were recorded in the range 400–3800 cm^{-1} on a MAGNA-IR 560 FT-IR instrument using KBr pellet technique. ^{29}Si MAS NMR experiments were performed on a Bruker Advance 400 spectrometer using a 5 mm-probe with a resonance frequency of 130.34 MHz at room temperature. X-ray photoelectron spectra (XPS) were recorded using a Thermo K-Alpha instrument with Al Kα X-ray radiation as the X-ray source.

Nitrogen adsorption–desorption isotherms were measured on a Micromeritics ASAP 2020 instrument at 77 K. The samples were degassed at 473 K for 2 h and 573 K under vacuum for 5 h prior to test. The total specific surface area was calculated using the Brunauer–Emmett–Teller (BET) equation, and the

micropore area and external surface area were determined by the t-plot method. The total pore volume was evaluated from the volume adsorbed at $P/P_0 = 0.99$. Whereas, the micropore volume and the mesopore volume were determined by the *t*-plot method and BJH method, respectively.

Synchrotron radiation SAXS experiments were carried out with Synchrotron radiation X-ray source at the 1W2A station in the Beijing Synchrotron Radiation Facility. The wavelength of incident X-ray (λ) was 0.154 nm. The distance of sample-to-detector was 1534 mm.

Temperature programmed reduction (TPR) experiments were carried out with purified mixture of N_2/H_2 (90/10 vol%) as a simultaneous carrier and reducing gas at a total flow rate of 40 mL min^{-1}. The signal was measured by a thermal conductivity detector and NiO (99.999%, Aldrich) was used for calibration of H_2 consumption.

X-ray absorption near edge structure (XANES) and extended X-ray absorption fine structure (EXAFS) were carried out with the 1W1B beamline, operated at 200 mA and 2.2 GeV in the Beijing Synchrotron Radiation Facility (BSRF). A Si (111) double-crystal monochromator was used to reduce the harmonic component of the monochromatic beam.

2.3 Catalytic activity

The series Cu/Y zeolite catalysts were tested in the total oxidation of toluene. The catalytic tests have been performed in a quartz fixed bed reactor. The catalyst (0.2 g), comminuted and sieved to a particle size of 420–841 μm, was placed on a quartz plug locating inside the reactor. The flow rate was set at 100 mL min^{-1} and the gas hourly space velocity (GHSV) was 30 000 mL g^{-1} h^{-1} at atmospheric pressure. Toluene dosing started by passing N_2 and O_2 mixture through a saturator (kept at 20 °C) to achieve the toluene vapor concentration of 1000 ppm in the reaction mixture. The catalytic tests were carried out from 200 to 450 °C in steps of 10 °C. Each temperature was maintained for 60 min before gas analysis. The toluene and oxidative products in the tail gas were analyzed by a gas chromatography (Shimadzu, GC 2014) equipped with three columns (Porapak-N and Molecular Sieve 13X for separation of CH_4, CO_2 and CO, OV-1 for separation of aromatic compounds), a methane reformer and two flame ionization detectors. The conversion of toluene was calculated by the concentration of toluene inlet and outlet. The catalytic activities were evaluated using T_{50} and T_{90}, which were defined as the temperatures required to attain 50% and 90% toluene conversion, respectively.

3 Results and discussion

3.1 Modifying aluminosilicate sol with CPT generating NaY-CPT zeolite

NaY zeolite synthesis, based on structure-directing method, usually use liquid water–glass as silica sources and aluminosilicate sol as seed solution (SDA). In this system, the highly active aluminosilicate species providing structural units is prerequisite for NaY zeolite growth.[32] NaY zeolite without CPT (NaY-con) and NaY-CPT zeolite with addition of CPT in the aluminosilicate sol as structure directing agent (SDA) were synthesized and their XRD patterns and crystallization curves are shown in Fig. 1. Both the NaY-CPT and NaY-con zeolites exhibit the same XRD patterns typical of Y zeolite structure (Fig. 1a), *i.e.* diffraction peaks diffraction peaks at 15.7°, 18.7°, 20.4°, 23.7°, 27.1°, 30.8°, 31.5° and 34.2° and none amorphous material is found.[33] The difference can be seen that NaY-con remains amorphous solid when crystallized for 12 hours and on diffraction peaks appear until 18 hours (Fig. 1b). While for NaY-CPT sample, the relatively crystallinity is more than 35% at 12 hours, indicating that CPT modified sol as SDA can shorten the crystallization induction period, and also improve growth of NaY zeolite. The crystallization time is shortened from 48 h (NaY-con) to 24 h (NaY-CPT). In addition, adopting solid silica as silicon source in an extremely dense aqueous system, NaY yield is up to 21–25% if compared to the conventional hydrothermal synthesis (10–12%).

The chloropropyl siloxane (CPT) as part of the silicon source forms the aluminosilicate in sol-CPT-1.0, thus chloropropyl group is covalently incorporated framework of NaY zeolite, due to Si–C bond in CPT not easy to cleavage, which affects the coordination and migration of aluminosilicate species, thus affecting the skeleton SiO_2/Al_2O_3 ratio of NaY zeolite. As shown

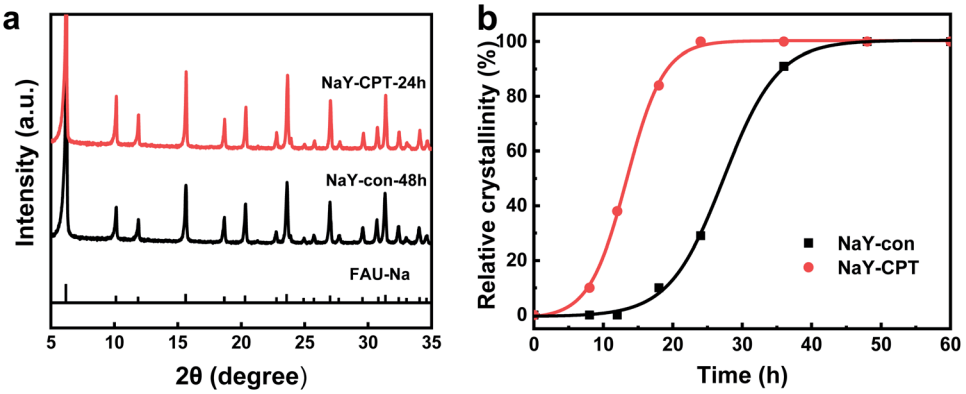

Fig. 1 XRD patterns (a) and crystallization curves (b) of NaY-con and NaY-CPT under different crystallization times.

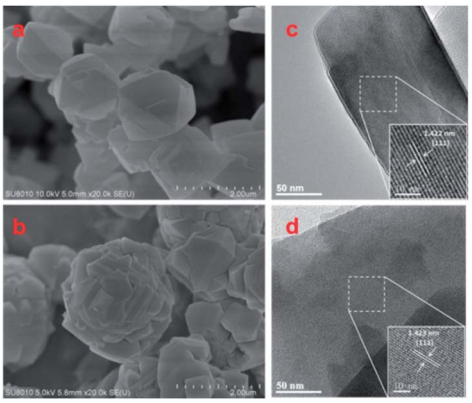

Fig. 2 SEM and TEM images of NaY-con (a and c) and NaY-CPT (b and d) zeolites.

in Fig. S1 and Table S1,† the SiO_2/Al_2O_3 ratio of the NaY-CPT (6.26) is higher than the NaY-con (5.35).

SEM images in Fig. 2a show that the NaY-con zeolite exhibits typical octahedral morphologies with the crystal size ranging from 500 to 800 nm. Adopting the sol-CPT-1.0, the NaY-CPT sample retains well-structured with the distinct angularity and octahedral morphologies. Notably, the crystal size of NaY-CPT decreases to 400–600 nm, then the well-aligned small crystals aggregate into a large dense particle with a particle about 2 μm in diameter (Fig. 2b). It suggests the CPT modified sol accelerates the zeolite crystallization, generating more small particles in a short period, resulting in a slight decrease in the crystal size and tending to aggregate into a large particle. The CPT impacts on the structure evolution of aluminosilicate sol, and the sol further as SDA to generate NaY zeolite aggregates. Specifically, addition of CPT in the aluminosilicate sol forms larger particles rapidly, which produces more active precursors to generate the well-aligned NaY aggregates. The modification of sol by CPT is discussed below. Transmission electron microscopy (TEM) studies reveal that the spacing between the lattice fringes was 1.423 nm, corresponding to the (111) crystal facet of FAU-Na zeolite (JCPDS PDF# 38–0239), as shown in Fig. 2c and d.

IR spectrum of NaY-CPT zeolite is basically consistent with NaY-con (Fig. S2a†). However, IR band at 788.6 cm^{-1} in NaY-con depending on Si/Al ratio slightly red-shifts to high frequencies (790.7 cm^{-1} in NaY-CPT). It suggests that the number of aluminium atoms in unit cell (N_{Al}) decreases, indicating that the Si/Al ratio of skeleton increases after chloropropyl modification. This is in line with the XRD characterization. Compared to the NaY-con, NaY-CPT sample has two extra peaks at 2854 and 2929 cm^{-1}, assigned to the C–H vibration derived from $-CH_3$ and $-CH_2-$ groups (Fig. S2b†). The structure of 3-chloropropyl-trimethoxysilane contains $ClCH_2-CH_2-CH_2-$ group linked by bonding SiO_x, the presence of chloride propyl-containing group in the zeolite can be proved. Furthermore, the STEM-energy dispersive X-ray (STEM-EDX) elemental mapping of NaY-CPT zeolite presents in Fig. S3.† It is obvious that Cl exists in the NaY-CPT zeolite and is evenly distributed.

The SAXS curves are depicted in Fig. 3. For qualitative analysis of SAXS data, the scattering curves are divided into three regions (I, II, III) according to different ranges of scattering vector magnitude q. The scattering curve at low q region (region I) is assigned to relatively larger particles or aggregates, while the high q region (regions II and III) is for the relatively small objects (monomers or dimers). The scattering curves of sol-con sample show that scattering curves at region I have a gradient ascent with the increase of aging time, which indicates that the relatively larger particles or aggregates gradually increase and the directing activity of sol as SDA also increase.[32] Different from the region I, the curves cross each other at region II and have a gradient descent at region III, demonstrating that monomers or dimers gradually decrease. Concave curves appeared in regions II and III indicated that the interactions among small species are small and can be negligible; *i.e.*, they are independent and long period is inexistent.

Different from sol-con, the scattering curves of the sol-CPT-1.0 close to each other in the three regions, which signifies that the directing activity of SDA is similar in the test time (Fig. 3b). During whole aging process, the order of magnitude of scattering intensity is 10^5 (sol-CPT-1.0) *vs.* 10^4 (sol-con), which reflects more aluminosilicate species in sol-CPT-1.0, suggesting adding CPT improves the formation of aluminosilicate species that exhibit high activity state as SDA.[34]

The difference in SAXS curves between the sol-CPT-1.0 and sol-con is related to particles aggregation states in terms of

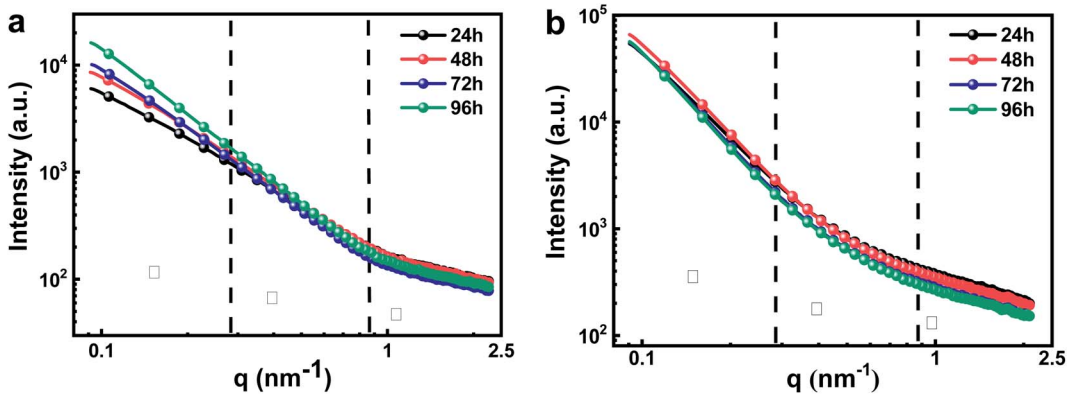

Fig. 3 Scattering curves of sol-con (a) and sol-CPT-1.0 (b) samples under different aging times.

fractal dimension of the species as shown in Fig. S4.† Herein, linear segments are determined on the SAXS curves in the q range $0.145 < q < 0.742$. With the sol aging, aluminosilicate species continue to grow, aggregate and the aluminosilicate polymers become denser and denser, resulting in a gradual increase in the fractal dimension.[35] It is believed that, in our previous work,[32] aluminosilicate sol was inactive or low activity for synthesizing NaY zeolite when the fractal dimension below 2.00 and it is high activity between 2.00 and 2.80, which all belong to mass fractal (denoted as D_m). For sol-CPT-1.0 in Fig. S4b,† the fractal dimension (negative slope of the curves) can fast reach 2.10 with aging 24 h, demonstrating that CPT modifier enables the sol species to reach a high active state rapidly. The active state of the sol means the species having the effective primary structure units for forming Y crystallite as identified in the following ^{29}Si NMR characterization. This can be proved by the fact that adding CPT modified SDA can promote nucleation and growth of NaY with well-crystallized structure. By contrast, the fractal dimension in sol-con as in Fig. S4a† changes continuously from 1.68 to 2.08 aging from 24 to 96 h. It confirms that the sol-con with D_m of 2.08 renders high activity. In other words, the aluminosilicate species in sol-con takes long aging time to reach an active state.

The scattering curves were analysed using the Monte Carlo method. This method assumes that the shape of particles is spherical. The Monte Carlo fitting results (Fig. S5a and b†) for the sol-con and sol-CPT-1.0 samples are consistent with the measured SAXS intensity profiles. The particle size distributions weighted by volume fraction as a function of sphere radius are shown in Fig. S4c and d.† Obviously, the analysis results illustrate the particle size dispersively distributed during the whole aging process. When the sol-con aging for 24 hours, there are very few particles larger than 10 nm and the large particles were not observed until 72 hours. In contrast, the larger particles are observed after 24 h aging time in the sol-CPT-1.0, which give an evidence again for the improvement of species particles in the sol-CPT-1.0.[36] This is consistent with the conclusion of fractal dimension described above. It is supposed that Si–OH is formed by hydrolysis of methoxy groups: $RSi(OCH_3)_3 + 3H_2O \rightarrow RSi(OH)_3 + 3CH_3OH$, which is easier to combine with the hydroxyl groups on the surface of inorganic substances and then provides the aluminosilicate entities as the zeolite subunits to grow Y crystals. Therefore, it can be considered that the addition of CPT can not only promote the growth of particles in the SDA, but also accelerate the crystallization process of NaY zeolite.

Fig. 4 shows the ^{29}Si NMR spectra of conventional sol and 1 mol% CPT modified sol. The chemical shifts at −71.6, −79.5, −81.6, −87.5 and −88.8 ppm are attributed to monosilicate, dipolysilicate, three-membered ring, four-membered ring and double three-membered ring, respectively.[37] Compared with sol-con, sol-CPT-1.0 appears peak splitting at −79.5, −81.6 and −87.5 ppm. This may be caused by the presence of two silicon sources in the system, one provided by inorganic silica gel and the other by organosiloxane, indicating that CPT can participate into the skeleton of aluminosilicate species in the system.

^{29}Si NMR spectra are analysed by the PeakFit software (Fig. S6†). After the peak area was normalized, the percentages

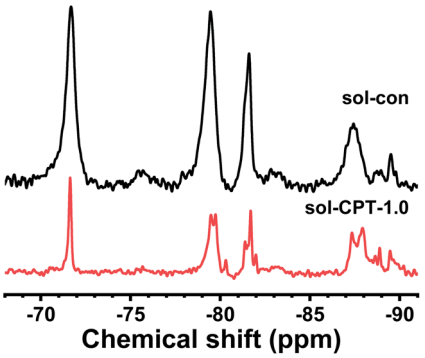

Fig. 4 ^{29}Si NMR spectra of sol-con and sol-CPT-1.0.

of each aluminosilicate species are compared and shown in Table S2.† The number of small particles such as monosilicate and dipolysilicate decrease after adding 1 mol% CPT into the sol. Moreover, the number of four-membered ring, six-membered ring and double four-membered ring with Si/Al is 1 or 2 also decrease. In contrast, three-membered ring, four-membered ring and double three-membered ring with Si/Al is 3 or pure silicon increase. The number of double six-membered ring (Si/Al is 2) should be reduced. Especially, a peak is found at −89.5 ppm related to new aluminosilicate species with octahedral cage which was considered as the nucleation center of FAU zeolite, forming by the double six-membered ring connecting the β cage.[37] These results indicate that CPT can promote aluminosilicate species forming large particles by consuming small particles and increase Si/Al ratio of species. This is associated with the results of SAXS and FT-IR characterization.

3.2 Promotive effect of CPT on performance of Cu/Y-CPT catalyst

After immobilizing Cu species on NaY-con and NaY-CPT zeolites *via* incipient wetness impregnation method, Cu/Y-5-con and Cu/Y-*x*-CPT were respectively obtained, and here, *x* refers to the content of Cu on the NaY zeolites. As seen in Fig. S10,† XRD patterns of the catalysts exhibit the typical Y zeolite structure with no amorphous material.[33] All samples show high crystallinity, indicating that loading Cu doesn't damage zeolite structure. Besides, adopting appropriate amount of copper (5–15 wt%) into Y zeolite supports, the diffraction lines corresponding to the CuO phase at 35.5° and 38.7° can be observed in the Cu/Y-5-con and Cu/Y-*x*-CPT catalysts.[38,39] The higher copper load, the stronger intensity of the diffraction peak of CuO can be observed. Scheme 1 illustrates the NaY-con and NaY-CPT zeolites as supports generating Cu-based active phase and perform different activity for toluene oxidation reaction.

N_2 adsorption–desorption isotherms show NaY zeolites and Cu/Y catalysts have type I isotherms typical for microporous characteristics (Fig. S11†). The texture parameters of the samples are listed in Table 1. After CPT modification, specific surface area of NaY-CPT increases slightly (from 689 to 726 m^2

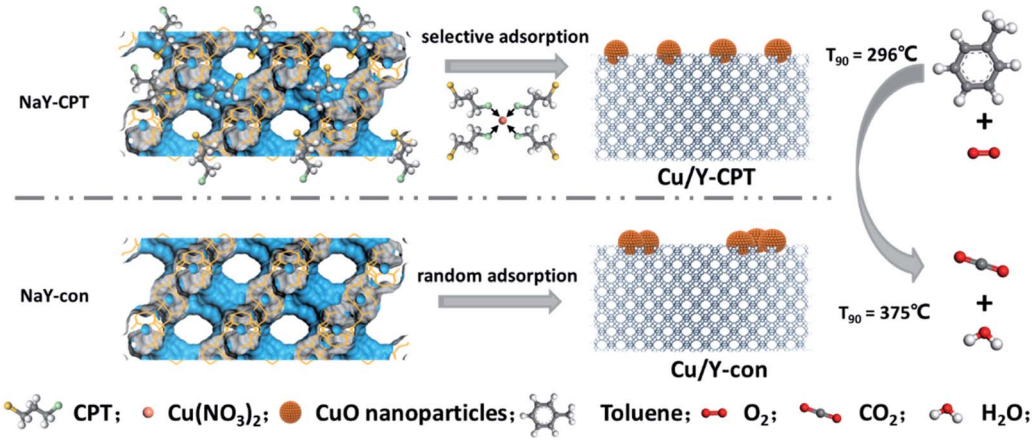

Scheme 1 Schematic illustration of the synthesis of Cu/Y-con and Cu/Y-CPT catalysts.

g^{-1}), which can be conjectured that NaY-CPT has a smaller particle size and thus exposes more crystal faces. The specific surface area of the Cu/Y samples is still high after Cu loading (514–628 $m^2\ g^{-1}$). Compared with the Cu/Y-5-con (570 $m^2\ g^{-1}$), Cu/Y-5-CPT has a larger specific surface area (628 $m^2\ g^{-1}$). Due to the chloropropyl functional group in the NaY-CPT zeolite, Cu species in the Cu/Y-5-CPT features high dispersion and consequently pore blockage is inhibited. Therefore, the specific surface area of Cu/Y-5-CPT decreases by 13.5% and that of Cu/Y-5-con by 17.3%. As the Cu loading increases, the specific surface area of the catalysts gradually decreases. It is worth noting that the external specific surface area of the CPT-modified catalysts is all higher than that of the unmodified catalyst. This is reasonable that Cu loading on the latter catalyst has more pore blockage, while CPT is beneficial to metal dispersivity. The high specific surface area of catalyst is of benefit to the increase of accessible sites, thereby improving the dispersibility of Cu species and catalytic activity as following discussion.

Fig. 5 shows TEM images of Cu/Y-5-con and Cu/Y-*x*-CPT (x = 5–15 wt%) catalysts. For Cu/Y-5-con catalyst, CuO nanoparticles are mainly dispersed on the edge of the zeolite surface, while CuO nanoparticles in Cu/Y-*x*-CPT catalysts prepared by CPT modified support are more evenly dispersed on the entire surface of zeolite. Clearly, CuO nanoparticles have a uniform particle size distribution between 2.0–4.0 nm in Cu/Y-*x*-CPT catalysts while 3.0–6.6 nm in Cu/Y-5-con catalyst. The HRTEM images of these catalysts give well-resolved lattice fringes of the copper oxides (Fig. S12†), showing the different lattice spacing of the (11–1) and (111) crystal planes at 0.252 and 0.232 nm respectively, in line with the corresponding d value of standard CuO (JCPDS PDF# 48–1548). This is supported by XRD characterization. Fig. S13† shows STEM-energy dispersive X-ray (STEM-EDX) elemental mapping of Cu/Y-5-con and Cu/Y-5-CPT catalysts. It is obvious that the full coverage of Cu in Cu/Y-5-CPT catalyst reveals high metal dispersion. However, the distribution of Cu species is not uniform in the Cu/Y-5-con catalyst and widely distributed on the edge of zeolite. These results demonstrate that the combination of CPT and metal can improve the dispersibility of CuO nanoparticles.

As seen in Fig. S14,† FT-IR spectra of Cu/Y-5-con and Cu/Y-*x*-CPT (x = 5–15 wt%) samples show the bands at 719 and 1020 cm^{-1}, assigned to the asymmetric and symmetric stretching vibrations of the inner TO_4 structure (T = Si, Al), respectively. However, Cu/Y-5-CPT has very lower intensity at 719 cm^{-1} band than that of Cu/Y-5-con. This is reasonable that the incorporation of CPT in Cu/Y-5-CPT catalyst, in combination of Cu species featuring small particle size, uniform species

Table 1 Texture properties of different Cu/Y samples

	Surface area ($m^2\ g^{-1}$)			Pore volume ($cm^3\ g^{-1}$)		
Sample	S_{BET}	S_{mic}	S_{ext}	V_{tot}	V_{mic}	V_{mes}
NaY-con	689	662	27	0.39	0.33	0.06
NaY-CPT	726	689	37	0.36	0.33	0.03
Cu/Y-5-con	570	544	26	0.30	0.27	0.03
Cu/Y-5-CPT	628	589	39	0.32	0.29	0.03
Cu/Y-10-CPT	543	508	35	0.28	0.25	0.03
Cu/Y-15-CPT	514	479	35	0.27	0.23	0.04

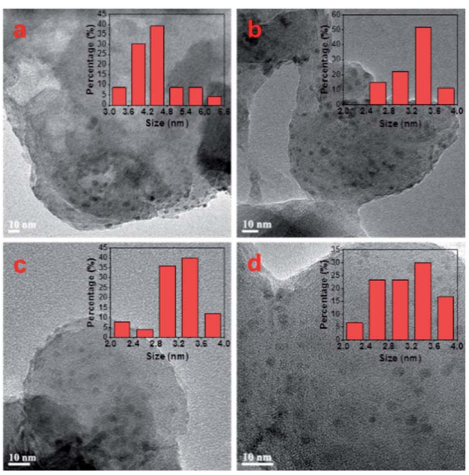

Fig. 5 TEM images of Cu/Y-5-con (a), Cu/Y-5-CPT (b), Cu/Y-10-CPT (c) and Cu/Y-15-CPT (d).

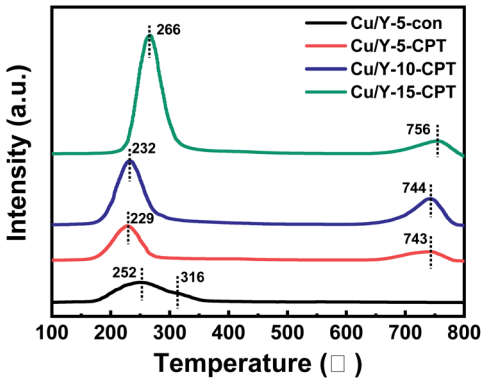

Fig. 6 H_2-TPR profile of Cu/Y-5-con and Cu/Y-*x*-CPT (*x* = 5–15 wt%).

distribution, thus can affect the vibration of the internal TO_4 structure. With the increase of copper content, the intensity of symmetric stretching vibrations of the inner TO_4 band gradually decreases. The band around 1140 cm^{-1} is assigned to the external tetrahedral (Si–O–T) asymmetric stretching vibration.[40] The band at 580 cm^{-1} is attributed to the double ring external linkage peak, which is considered as double six-membered ring vibration of NaY zeolite crystals. The 462 cm^{-1} band is assigned to internal tetrahedral (O–T–O) bending vibrations. NaY zeolite IR spectra has notable features of double ring external linkage vibration at 580 cm^{-1} and external tetrahedral symmetric stretching vibration at 789 cm^{-1}. All the Cu/Y-*x*-CPT catalysts have no peak shift, illuminating that the framework units of zeolite almost unchanged after the organo-modification.[41]

The H_2-TPR measurement shown in Fig. 6 displays that the Cu/Y-5-con and Cu/Y-*x*-CPT samples have different reduction peaks between 200 °C and 800 °C. The peaks centered at relatively lower temperatures (252 °C, 229 °C, 232 °C and 266 °C) should be assigned to the reduction of $(Cu–O–Cu)^{2+}$ and isolated Cu^{2+}, which are highly dispersed Cu species. The peaks centered at relatively higher temperatures (316 °C, 743 °C, 744 °C and 756 °C) were ascribed to the reduction of Cu^{+} to Cu^{0}.[39,42,43] The samples present both peaks but at different temperatures and relative intensities, probably due to the different interaction between the copper species and zeolite support.[44–46]

Compared with Cu/Y-5-con, Cu/Y-5-CPT and Cu/Y-10-CPT exhibit a lower H_2-TPR reduction peak temperature (252 °C *vs.* 229 °C and 232 °C) and therefore latter both samples have higher redox ability. Owing to the CPT functional groups, the –Cl group containing lone pair electrons is beneficial to interacting with the copper species, thus forming uniform Cu small particles. Cu/Y-*x*-CPT series display a higher H_2-TPR reduction peak at 743–756 °C, indicating the strong interaction exists between copper species and NaY-CPT zeolite support, which might affect the reaction activity and stability.

The hydrogen consumption in the TPR measurements is listed in Table 2. It is observed that the H_2/Cu ratios of the Cu/Y-5-CPT and Cu/Y-10-CPT catalysts are 0.94 and 0.95 respectively, meaning that almost all of the Cu^{2+} can be reduced to Cu^{0} in these catalysts according to stoichiometry. While the Cu/Y-5-con catalyst, allows the H_2/Cu ratio of 0.72, indicating that only three-quarter of copper is completely reduced. Therefore, it is proved that the CPT modification is beneficial to improve the reduction ability of the catalyst. On the other hand, Cu/Y-15-CPT catalyst gives H_2/Cu ratio of 0.85 and H_2-TPR reduction peak temperature at 266 °C, higher than the Cu/Y-5-con catalyst (252 °C). This is probably the excessive Cu species present in a freedom state on the zeolite.

X-ray absorption near edge structure (XANES) spectra (Fig. 7a) and extended X-ray absorption fine structure (EXAFS) (Fig. 7b) direct provide the structure information of the metal oxide loading on the zeolite. As seen in Fig. 7a, the XANES spectra of Cu/Y catalysts and reference CuO_x samples demonstrate a sharp absorption at about 9000–9001 eV due to the electronic transition from 1s to 4p of Cu^{2+} species.[47] This result shows that the Cu-loaded catalysts are mainly Cu^{2+} and no obvious pre-edge feature of Cu^{+} (8998–8999 eV) can be observed. The shoulder at about 8988–8989 eV in Cu/Y catalysts also proves the existence of the CuO-like structure, which is in line with the XRD and TEM results. The Fourier transform moduli of the Cu K-edge EXAFS spectra of the Cu/Y catalysts and reference CuO_x samples are presented in Fig. 7b. The third coordination of all Cu/Y catalysts at the distance of 3.35 Å is similar to that of CuO sample, which also indicates that the copper oxide in catalysts mainly exist in the form of Cu^{2+}. In addition, the strength of the fourth, fifth and sixth coordination layer of the Cu/Y catalysts is lower than that of CuO sample, illustrating that the coordination layers have lower saturation, that is, smaller particles and better dispersion of CuO nanoparticles in catalysts.

The Cu 2p spectra of Cu/Y catalysts are shown in Fig. 8a. Two peaks are observed at 932.5–936 eV and 952.5–956 eV, which correspond to Cu $2p_{3/2}$ and Cu $2p_{1/2}$ respectively. Furthermore, the presence of two shake-up satellite peaks in the range of 940–

Table 2 Reducibility and reaction performance of Cu/Y-5-con and Cu/Y-*x*-CPT samples

	H_2-TPR				Toluene conversion	
Sample	T_1 °C	T_2 °C	H_2-uptake mmol H_2 g^{-1}	H_2/Cu molar ratio	T_{50} °C	T_{90} °C
Cu/Y-5-con	252	316	0.56	0.72	315	375
Cu/Y-5-CPT	229	743	0.73	0.94	295	335
Cu/Y-10-CPT	232	744	1.48	0.95	280	296
Cu/Y-15-CPT	266	756	1.99	0.85	291	318

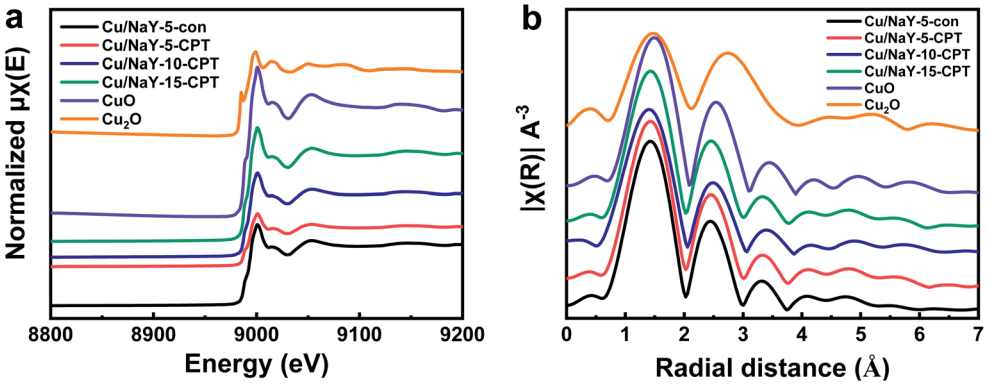

Fig. 7 Normalized Cu K-edge XANES spectra (a) and magnitude of FourierFourier transformed EXAFS spectra (b) of Cu/Y catalysts along with the Cu^{2+} and Cu^{+} reference compounds (CuO and Cu_2O). The spectra are displaced vertically for clarity.

945 eV and 960–965 eV confirms Cu^{2+} in the Cu/Y catalysts.[48] There are two types of Cu^{2+} species in the catalysts. The spectra of Cu $2p_{3/2}$ can be deconvolved into two peaks at 935.2 eV and 933.1 eV, which are attributed to isolated Cu^{2+} species and agglomerated CuO nanoparticles.[49,50] The isolated Cu^{2+} species coordinate surface oxygen atoms, while the agglomerated CuO nanoparticles are located on the surface of catalysts, as demonstrated by the XRD characterization. These results are consistent with H_2-TPR measurements, which indicate both isolated Cu^{2+} species and CuO nanoparticles might be present in the Cu/Y catalysts. The peak area ratios of isolated Cu^{2+} to CuO crystallites in the XPS spectra are calculated and shown in Table 3. It can be seen that the surface concentrations of isolated Cu^{2+} on the Cu/Y-5-CPT catalysts are higher than that on the Cu/Y-5-con catalyst, therefore the former has better reduction ability.

The O 1s spectra show one band assigned to lattice oxygen O_{latt} (529.2 eV) and a separate band attributed to adsorbed oxygen species O_{abs} (532.2 eV) adjacent to oxygen vacancies (Fig. 8b). The percentages of $O_{ads}/(O_{ads} + O_{latt})$ are shown in Table 3. As seen, all the Cu/Y-CPT catalysts have higher surface oxygen vacancy concentration with the $O_{ads}/(O_{ads} + O_{latt})$ ratio above 81% than Cu/Y-5-con (73.8%). Since the adsorbed oxygen species are more reactive than lattice oxygen species in the oxidation reaction due to their high mobility,[21] CPT modified catalysts have higher catalytic activity as following evaluation in the toluene oxidation reaction.

3.3 Catalytic evaluation

The Cu/Y-5-con and Cu/Y-*x*-CPT catalysts were evaluated for the total toluene oxidation by monitoring the conversion as function of the temperature (light-off curve). Two parameters, the temperatures required to attain 50% (T_{50}) and 90% (T_{90}) toluene conversion, are used to evaluate catalytic activities for toluene oxidation. The T_{50} and T_{90} data for the studied catalysts are illustrated in Fig. 9 and Table 2. The Cu-containing NaY zeolites show very high selectivity to CO_2, only small traces of benzene and CO (yield below 1%) at temperatures lower than 300 °C. Obviously, the catalyst matrix, which possesses different specific surface area, metal dispersion, redox ability and active oxygen species in the studied materials, influences the reactive

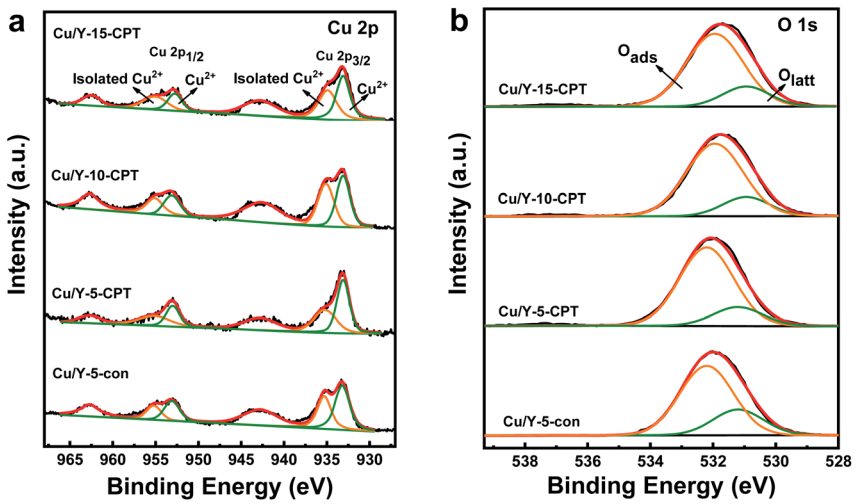

Fig. 8 X-ray photoelectron spectra for Cu 2p (a) and O 1s (b) of Cu/Y catalysts.

Table 3 XPS results of the Cu/Y catalysts

	Cu $2p_{3/2}$ (B. E.)		Cu $2p_{1/2}$ (B. E.)			
Sample	CuO	*Iso*-Cu^{2+}	CuO	*Iso*-Cu^{2+}	*Iso*-Cu^{2+}/(*Iso*-Cu^{2+} + CuO)	$O_{abs}/(O_{abs} + O_{latt})$
Cu/Y-5-con	933.2	935.3	953.1	955.2	41.7%	73.8%
Cu/Y-5-CPT	933.1	935.2	953.0	955.1	46.3%	81.9%
Cu/Y-10-CPT	933.1	935.1	953.1	955.1	49.7%	81.8%
Cu/Y-15-CPT	933.1	934.9	952.8	955.1	49.1%	81.3%

activity. At temperature of 275 °C, the conversion over Cu/Y-5-con and Cu/Y-5-CPT are 21.0% and 26.5%, respectively (Fig. 9a). The Cu/Y-5-CPT catalyst performs the T_{90} of 335 °C while the value is 375 °C for Cu/Y-5-con, which demonstrates that after introducing CPT on NaY zeolite the catalytic performance is significantly improved.

It is reasonable that Cu/Y-5-CPT catalyst possesses higher specific surface area, better metal dispersity and richer adsorbed oxygen species, which results in higher catalytic activity than Cu/Y-5-con. The -Cl functional groups in NaY-CPT significantly promotes complexation between Cu metal and zeolite surface, leading to high reducibility of Cu species, as observed in the H_2-TPR experiments. Thus, Cu/Y-5-CPT catalyst present higher activity probably due to higher Cu species dispersion, more *iso*-Cu^{2+} and richer adsorbed oxygen species on Cu/Y-5-CPT catalyst than on Cu/Y-5-con. Similar results have been described for other reactions. Deng *et al.* prepared 35$LaCoO_3$/SBA-15 catalyst by *in situ* method and found that the high dispersion of $LaCoO_3$ was conducive to the adsorption and activation of toluene.[51] Peng *et al.* found that the reducibility of catalyst and active oxygen species had a great impact on the reaction activity, especially the adsorbed oxygen in reactive oxygen species.[21]

The effect of Cu contents on toluene catalytic activity was investigated on the NaY-*x*-CPT catalysts. The Cu/Y-10-CPT catalyst exhibits the best performance (T_{90} = 296 °C), which T_{90} of Cu/Y-5-CPT and Cu/Y-15-CPT is 335 °C and 318 °C, respectively. Obviously, the proper Cu content (10 wt%) is beneficial to catalytic oxidation activity. Although the specific surface area of Cu/Y-10-CPT catalyst is lower than Cu/Y-5-CPT, their redox ability and ratios of isolated Cu^{2+} are similar, which indicating that the catalyst still maintains a high metal dispersion when the Cu content increases to 10 wt%. Cu/Y-10-CPT catalyst can provide more catalytic activity sites, so its activity is higher than that of Cu/Y-5-CPT. It can be seen from the texture properties, Cu/Y-15-CPT catalyst gives lower specific surface area, due to the presence of pore blocking phenomenon when the Cu load is excessive. As increasing Cu content to 15 wt%, the contact area between reactants and catalyst decreases, thus leading to lower catalytic activity than the Cu/Y-10-CPT catalyst. Furthermore, as shown in Fig. 6, the Cu/Y-15-CPT catalyst has the highest reduction temperature (266 °C) compared with the Cu/Y-5-CPT (229 °C) and Cu/Y-10-CPT catalysts (232 °C), which indicates that the Cu/Y-15-CPT catalyst has poor reducibility. In addition, the H_2/Cu ratio in Cu/Y-15-CPT catalyst (0.85) is lower than other two catalysts with the less Cu contents (0.94, 0.95), which means that copper in the Cu/Y-15-CPT catalyst cannot be completely reduced before 800 °C. Therefore, the super catalytic activity on Cu/Y-*x*-CPT is strongly related to appropriate copper content. Cu/Y-5-con and Cu/Y-10-CPT catalysts were tested isothermally under 300 °C with reaction time and the dependence of the catalytic conversion on time was shown in Fig. 9b. Cu/Y-10-CPT exhibits higher catalytic activity than other catalysts, maintaining approximately 98.0% conversion during 360 min of reaction period. All the samples present high stability without noticeable deactivation in the toluene oxidation reaction.

It is generally believed that the introduction of water vapor into the feed gas has an important effect on the catalytic activity.[52] Since industrial waste gas often contains a certain

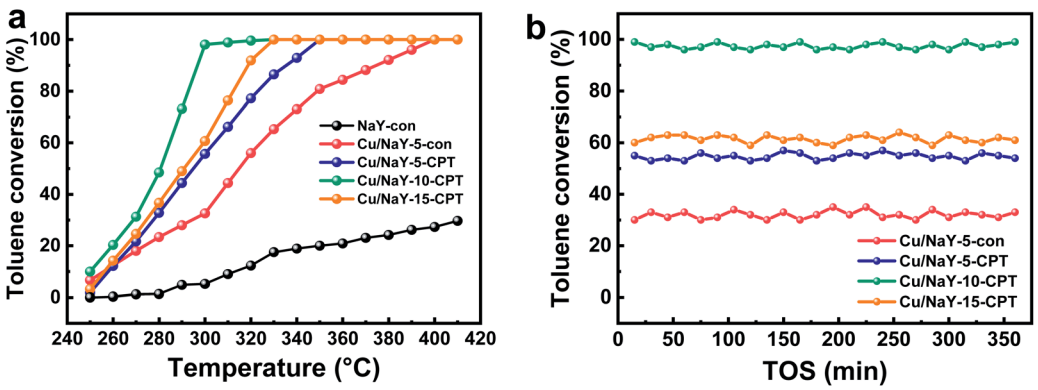

Fig. 9 Catalytic activity as a function of temperature (a) and time on stream at 300 °C (b) for Cu/Y catalysts.

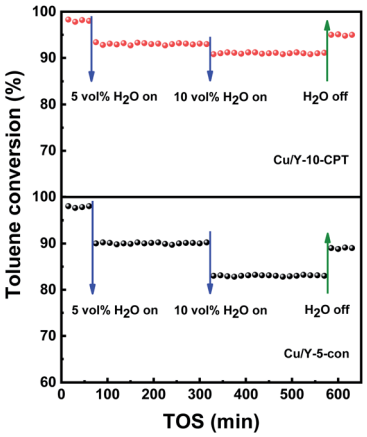

Fig. 10 Toluene conversion over Cu/Y-5-con and Cu/Y-10-CPT catalysts in the presence or absence of water vapor at 395 °C and 300 °C respectively.

concentration of water vapor, the influence of water vapor on the catalytic activity of the Cu/Y-5-con and Cu/Y-10-CPT catalysts has been tested with 5.0 and 10.0 vol% water vapor. When the 5.0 vol% water vapor was introduced into the feed gas, the toluene conversion reduced from 98.0% to 93.2% (Cu/Y-10-CPT) and 90.1% (Cu/Y-5-con), respectively (Fig. 10). When rising the water vapor content to 10.0 vol%, the toluene conversion decreases to 91.4% and 83.0%, respectively. Therefore, water vapor plays a negative role in toluene oxidation because of the competitive adsorption between toluene and water vapor.[53] However, after water vapor was cut off, the toluene conversion restores to 95.0% (Cu/Y-10-CPT) and 89.2% (Cu/Y-5-con). These results show that the structural integrity of the Cu/Y-10-CPT catalyst remains better than Cu/Y-5-con in the long-term running test. Fig. S15† shows TEM images of the Cu/Y-10-CPT catalyst before and after toluene oxidation reaction under water vapor condition. After the reaction, the metal particle size distribution of the catalyst is 2.0–4.5 nm, which is slightly higher than that fresh catalyst (2.0–4.0 nm). H_2-TPR profiles of fresh and used catalyst are presented in Fig. S16.† Compared to the fresh Cu/Y-10-CPT catalyst, the used catalyst shifts to the high temperature (from 232 to 243 °C), indicating that reducibility decreases. On the contrast, the used Cu/Y-5-con catalyst also shifts to the high temperature (252 and 316 to 296 and 334 °C), the margin of temperature rising is larger than the used Cu/Y-10-CPT catalyst. In addition, for the peak at higher temperature area, it shifts to low temperature direction (744 to 701 °C), showing that the interaction between metal and zeolite support is weakened. Therefore, after cutting off the water vapor, the toluene conversion cannot recover to the original level even though catalysts retain its structural integrity. This is consistent with the literature result.[54] The toluene conversion over Cu/Y-10-CPT catalyst drops 3.0% less than that of Cu/Y-5-con (8.8%) after cut off water vapor. These results suggest that Cu species have higher stability after incorporating to the CPT in Y zeolite.

Accordingly, the mechanism of toluene oxidation over the copper-based catalysts can be explained by the Mars-van Krevelen (MVK) mechanism.[55,56] It was proved that toluene reacted with the active oxygen species according to the O 1s spectra (Fig. 8). Toluene first reacted with the active oxygen species at the Cu/Y catalyst interface to form intermediate species. Cu/Y catalyst is reduced, meanwhile, generating the oxygen vacancy. Then intermediate species can further react with active oxygen species to form CO_2 and H_2O. Finally, the active oxygen species could be supplemented by gas phase oxygen. As a result, the oxygen vacancy is filled by oxygen from the feed gas and the reduced site is regenerated. Therefore, it is apparent that both lattice oxygen and adsorbed oxygen species contribute the catalytic oxidation. On the one hand, the Cu/Y-CPT catalysts with the higher concentration of adsorbed oxygen species display higher activity than Cu/Y-5-con catalyst, which proves the adsorbed oxygen species more active. The rich adsorbed oxygen species provides higher mobility for the oxidation of toluene molecules. On the other hand, the good metal dispersion in the Cu/Y-CPT catalysts provides high reducibility. In order to test the role of the –Cl groups, NaY-CPT zeolite was calcined before Cu-impregnation, the catalyst, denoted as Cu/Y-5-CPT-calcined had relatively poor performance. The textural properties and catalytic performance of Cu/Y-5-CPT-calcined are described in the ESI.†

As known, the noble metal-loaded FAU zeolites described in previous literature has high toluene conversion.[57] The T_{90} of Pd-FAU catalyst was even below 200 °C under the conditions of 1000 ppm toluene and 60 000 h^{-1}. The application of transition metal-based catalyst usually results in higher value of T_{50} or/and T_{90}. Nevertheless, the Cu/Y-CPT catalysts showed great application prospects in the toluene oxidation among other transition metal-containing zeolite catalysts. Their activity is noticeably higher compared to other catalysts reported in the literature (Table S4†), such as Co-, Mn- and Nb-containing zeolites (BEA and clinoptilolite and MWW) under the same experimental conditions, which gave the similar conversion of toluene at much higher temperatures (T_{90} > 320 °C).[10,22,58,59] In addition, NaY zeolite as support presents high stability without noticeable deactivation in the oxidation reaction, while CuKIL samples show 9–23% toluene conversion loss in the initial 75 min of reaction.[55] Therefore, Cu-based NaY catalysts modified by other organic groups deserve careful research for VOCs catalytic oxidation.

4 Conclusions

A new strategy has been carried out for achieving NaY-CPT zeolite by modifying sol with 3-chloropropyl-trimethoxysilane (CPT) as structure directing agent (SDA) in a condensed synthetic system *via* solid silica source. Incorporating CPT in the aluminosilicate sol can effectively accelerate formation of building active unit and improve the ratio of Si/Al of NaY zeolite, meanwhile zeolite yield is twice as much in this system. NaY-CPT zeolite displays well-aligned octahedral and small crystals structure with high surface area and external surface area. The catalytic activity is evaluated over Cu/Y catalysts before and after CPT modification in the total toluene oxidation. The Cu/Y-CPT catalysts perform high reactivity and stability for the toluene oxidation, even with water vapor condition. The complexation

of copper with CPT modified NaY zeolite can improve the Cu species load and enhance Cu species forming smaller size and oxidation property, leading to high dispersity and large proportion of adsorbed oxygen species. The optimal Cu/Y-10-CPT catalyst performs the highest activity with T_{90} of 296 °C, while the value is 375 °C for Cu/Y-5-con.

These results approve the combination of specific surface area, redox properties, metal dispersion and adsorbed oxygen species are the key factors to design active catalyst for toluene oxidation reaction. For scale-up effect, the transition metal Cu coupled with the NaY-CPT as support will generate a high effective and low-cost VOCs oxidation catalyst.

Author contributions

X. L. Meng designed the experiments, synthesized the catalysts, performed all the characterizations, and conducted toluene oxidation testing. All co-authors contributed to data analyses and discussion. X. L. Meng wrote the initial manuscript. Y. J. Gong wrote the final version. Prof. Y. J. Gong directed and coordinated the project.

Conflicts of interest

There are no conflicts to declare.

Acknowledgements

The work was supported by the National Natural Science Foundation of China [22078356, U1662116, U1910206]; and the Foundation of State Key Laboratory of Coal Conversion [Grant No. J20-21-602, J21-22-604].

Notes and references

1 Q. Wang, K. L. Yeung and M. A. Banares, *Catal. Today*, 2020, **356**, 141–154.
2 L. Zhang, Y. Peng, J. Zhang and L. Chen, *Chin. J. Catal.*, 2016, **37**, 800–809.
3 G. Wang, Z. Zhang, J. Wang, N. Li and Z. Hao, *Ind. Eng. Chem. Res.*, 2015, **54**, 1074–1080.
4 X. Zhang, B. Gao, A. E. Creamer, C. Cao and Y. Li, *J. Hazard. Mater.*, 2017, **338**, 102–123.
5 A. H. Mamaghani, F. Haghighat and C.-S. Lee, *Appl. Catal., B*, 2017, **203**, 247–269.
6 R. López-Fonseca, J. Gutiérrez-Ortiz and J. González-Velasco, *Appl. Catal., A*, 2004, **271**, 39–46.
7 T. Cai, H. Huang, W. Deng, Q. Dai, W. Liu and X. Wang, *Appl. Catal., B*, 2015, **166–167**, 393–405.
8 C. Chen, J. Zhu, F. Chen, X. Meng, X. Zheng, X. Gao and F.-S. Xiao, *Appl. Catal., B*, 2013, **140**, 199–205.
9 Z. Zhang, L. Xu, Z. Wang, Y. Xu and Y. Chen, *J. Nat. Gas Chem.*, 2010, **19**, 417–421.
10 A. Rokicińska, M. Drozdek, B. Dudek, B. Gil, P. Michorczyk, D. Brouri, S. Dzwigaj and P. Kustrowski, *Appl. Catal., B*, 2017, **212**, 59–67.
11 J. Hou, Y. Li, L. Liu, L. Ren and X. Zhao, *J. Mater. Chem. A*, 2013, **1**, 6736–6741.
12 W. Si, Y. Wang, P. Yue, L. Xiang and J. Li, *Chem. Commun.*, 2015, **51**, 14977–14980.
13 N. Blanch-Raga, M. D. Soriano, A. E. Palomares, P. Concepción, J. Martínez-Triguero and J. Nieto, *Appl. Catal., B*, 2013, **130–131**, 36–43.
14 B. de Rivas, N. Guillen-Hurtado, R. Lopez-Fonseca, F. Coloma-Pascual, A. Garcia-Garcia, J. I. Gutierrez-Ortiz and A. Bueno-Lopez, *Appl. Catal., B*, 2012, **121**, 162–170.
15 Y. Wu, Y. Zhang, M. Liu and Z. Ma, *Catal. Today*, 2010, **153**, 170–175.
16 M. Zimowska, A. Michalik-Zym, R. Janik, T. Machej, J. Gurgul, R. P. Socha, J. Podobinski and E. M. Serwicka, *Catal. Today*, 2007, **119**, 321–326.
17 Z. Yan, Z. Xu, J. Yu and M. Jaroniec, *Appl. Catal., B*, 2016, **199**, 458–465.
18 W. B. Li, J. X. Wang and H. Gong, *Catal. Today*, 2009, **148**, 81–87.
19 Y. Wu, M. Liu, Z. Ma and T. X. Sheng, *Catal. Today*, 2011, **175**, 196–201.
20 N. Blanch-Raga, A. E. Palomares, J. Martinez-Triguero and S. Valencia, *Appl. Catal., B*, 2016, **187**, 90–97.
21 Y. Peng, L. Zhang, L. Chen, D. Yuan, G. Wang, X. Meng and F.-S. Xiao, *Catal. Today*, 2017, **297**, 182–187.
22 Z. Ozcelik, G. S. P. Soylu and I. Boz, *Chem. Eng. J.*, 2009, **155**, 94–100.
23 T. Barakat, J. C. Rooke, H. L. Tidahy, M. Hosseini, R. Cousin, J.-F. Lamonier, J.-M. Giraudon, G. DeWeireld, B. LianSu and S. Siffert, *Chemsuschem*, 2011, **4**, 1420–1430.
24 J. I. Gutierrez-Ortiz, R. Lopez-Fonseca, U. Aurrekoetxea and J. R. Gonzalez-Velasco, *J. Catal.*, 2003, **218**, 148–154.
25 A. Z. Abdullah, M. Bakar and S. Bhatia, *J. Hazard. Mater.*, 2006, **129**, 39–49.
26 G. S. P. Soylu, Z. Ozcelik and I. Boz, *Chem. Eng. J.*, 2010, **162**, 380–387.
27 Y. Meng, H. C. Genuino, C.-H. Kuo, H. Huang, S.-Y. Chen, L. Zhang, B. A. Rossi and S. L. Suib, *J. Am. Chem. Soc.*, 2013, **135**, 8594–8605.
28 A. P. Antunes, M. F. Ribeiro, J. M. Silva, F. R. Ribeiro, P. Magnoux and M. Guisnet, *Appl. Catal., B*, 2001, **33**, 149–164.
29 D. Romero, D. Chlala, M. Labaki, S. Royer, J. P. Bellat, I. Bezverkhyy, J. M. Giraudon and J. F. Lamonier, *Catalysts*, 2015, **5**, 1479–1497.
30 W. Fu, Z. Lei, T. Tang, Q. Ke, S. Wang, J. Hu, G. Fang, J. Li and F. S. Xiao, *J. Am. Chem. Soc.*, 2011, **133**, 15346–15349.
31 B. A. Holmberg, H. Wang, J. M. Norbeck and Y. Yan, *Microporous Mesoporous Mater.*, 2003, **59**, 13–28.
32 X. Zhao, R. Liu, H. Zhang, Y. Shang, Y. Song, C. Liu, T. Wang, Y. Gong and Z. Li, *J. Appl. Crystallogr.*, 2017, **50**, 231–239.
33 A. D3906-03, *Standard Test Method for Determination of Relative X-ray Diffraction Intensities of Faujasite-Type Zeolite-Containing Materials*, ASTM International, West Conshohocken PA, 2003.

34 C. Gommes, S. Blacher, B. Goderis, R. Pirard, B. Heinrichs, C. Alie and J. P. Pirard, *J. Phys. Chem. B*, 2004, **108**, 8983–8991.
35 T. M. Stawski, S. A. Veldhuis, R. Besselink, H. L. Castricum, G. Portale, D. H. A. Blank and J. E. ten Elshof, *J. Phys. Chem. C*, 2011, **115**, 20449–20459.
36 H. Nirschl and X. Guo, *Chem. Eng. Res. Des.*, 2018, **136**, 431–446.
37 C. Li, PhD thesis, Jilin University, 2009.
38 M. Piumetti, S. Bensaid, T. Andana, N. Russo, R. Pirone and D. Fino, *Appl. Catal., B*, 2017, **205**, 455–468.
39 U. De la Torre, M. Urrutxua, B. Pereda-Ayo and J. R. Gonzalez-Velasco, *Catal. Today*, 2016, **273**, 72–82.
40 X. Zhang, Q. Guo, B. Qin, Z. Zhang, F. Ling, W. Sun and R. Li, *Catal. Today*, 2010, **149**, 212–217.
41 J. Zhao, Y. Yin, Y. Li, W. Chen and B. Liu, *Chem. Eng. J.*, 2016, **284**, 405–411.
42 S. Fan, J. Xue, T. Yu, D. Fan, T. Hao, M. Shen and W. Li, *Catal. Sci. Technol.*, 2013, **3**, 2357–2364.
43 B. Dou, G. Lv, C. Wang, Q. Hao and K. Hui, *Chem. Eng. J.*, 2015, **270**, 549–556.
44 L. Capek, J. Dedecek, B. Wichterlova, L. Cider, E. Jobson and V. Tokarova, *Appl. Catal., B*, 2005, **60**, 147–153.
45 R. Lopez-Fonseca, B. de Rivas, J. I. Gutierrez-Ortiz, A. Aranzabal and J. R. Gonzalez-Velasco, *Appl. Catal., B*, 2003, **41**, 31–42.
46 H. Valdes, V. A. Solar, E. H. Cabrera, A. F. Veloso and C. A. Zaror, *Chem. Eng. J.*, 2014, **244**, 117–127.
47 X. Wang, A. A. Arvidsson, M. O. Cichocka, X. Zou, N. M. Martin, J. Nilsson, S. Carlson, J. Gustafson, M. Skoglundh, A. Hellman and P.-A. Carlsson, *J. Phys. Chem. C*, 2017, **121**, 27389–27398.
48 M. C. Biesinger, L. W. M. Lau, A. R. Gerson and R. S. C. Smart, *Appl. Surf. Sci.*, 2010, **257**, 887–898.
49 A. E. Palomares, C. Franch and A. Corma, *Catal. Today*, 2011, **176**, 239–241.
50 H. L. Tidahy, S. Siffert, J. F. Lamonier, R. Cousin, E. A. Zhilinskaya, A. Aboukais, B. L. Su, X. Canet, G. De Weireld, A. Frere, J. M. Giraudon and G. Leclercq, *Appl. Catal., B*, 2007, **70**, 377–383.
51 J. Deng, L. Zhang, H. Dai and C.-T. Au, *Appl. Catal., A*, 2009, **352**, 43–49.
52 S. Xie, J. Deng, S. Zang, H. Yang, G. Guo, H. Arandiyan and H. Dai, *J. Catal.*, 2015, **322**, 38–48.
53 Y. Liu, H. Dai, J. Deng, S. Xie, H. Yang, W. Tan, W. Han, Y. Jiang and G. Guo, *J. Catal.*, 2014, **309**, 408–418.
54 Y. Guo, D.-P. Yang, M. Liu, X. Zhang, Y. Chen, J. Huang, Q. Li and R. Luque, *J. Mater. Chem. A*, 2019, **7**, 8832–8844.
55 P. Djinovic, A. Ristic, T. Zumbar, V. D. B. C. Dasireddy, M. Rangus, G. Drazic, M. Popova, B. Likozar, N. Z. Logar and N. N. Tusar, *Appl. Catal., B*, 2020, **268**, 118749.
56 H. Huang, Y. Xu, Q. Feng and D. Y. C. Leung, *Catal. Sci. Technol.*, 2015, **5**, 2649–2669.
57 Y. Zhang, Z. Si, J. Gao, Y. Liu, L. Liu, X. Wu, R. Ran and D. Weng, *Appl. Surf. Sci.*, 2019, **469**, 246–252.
58 A. G. M. da Silva, H. V. Fajardo, R. Balzer, L. F. D. Probst, A. S. P. Lovon, J. J. Lovon-Quintana, G. P. Valenca, W. H. Schreine and P. A. Robles-Dutenhefner, *J. Power Sources*, 2015, **285**, 460–468.
59 A. J. Schwanke, R. Balzer, C. W. Lopes, D. M. Meira, U. Diaz, A. Corma and S. Pergher, *Chem. Eur J.*, 2020, **26**, 10459–10470.